Title

Probing the mechanism of CO 2 capture in diamine-appended metal—organic frameworks using measured and simulated X-ray spectroscopy



Journal

Physical Chemistry Chemical Physics, 17(33)

ISSN

0956-5000

Authors

Drisdell, Walter S

Poloni, Roberta

McDonald, Thomas M

et al.

Publication Date

2015-09-07

DOI

10.1039/c5cp02951a

Peer reviewed

PCCP

PAPER

View Article Online
View Journal | View Issue



Cite this: *Phys. Chem. Chem. Phys.*, 2015, **17**, 21448

# Probing the mechanism of $CO_2$ capture in diamine-appended metal–organic frameworks using measured and simulated X-ray spectroscopy†

Walter S. Drisdell,[a] Roberta Poloni,[b] Thomas M. McDonald,[c] Tod A. Pascal,[d] Liwen F. Wan,[d] C. Das Pemmaraju,[d] Bess Vlaisavljevich,[e] Samuel O. Odoh,[f] Jeffrey B. Neaton,[d] Jeffrey R. Long,[ac] David Prendergast[d] and Jeffrey B. Kortright*[a]

Received 22nd May 2015,
Accepted 15th July 2015

DOI: 10.1039/c5cp02951a

www.rsc.org/pccp

Diamine-appended metal–organic frameworks display great promise for carbon capture applications, due to unusual step-shaped adsorption behavior that was recently attributed to a cooperative mechanism in which the adsorbed $CO_2$ molecules insert into the metal–nitrogen bonds to form ordered ammonium carbamate chains [McDonald *et al.*, *Nature*, 2015, **519**, 303]. We present a detailed study of this mechanism by *in situ* X-ray absorption spectroscopy and density functional theory calculations. Distinct spectral changes at the N and O K-edges are apparent upon $CO_2$ adsorption in both mmen-$Mg_2$(dobpdc) and mmen-$Mn_2$(dobpdc), and these are evaluated based upon computed spectra from three potential adsorption structures. The computations reveal that the observed spectral changes arise from specific electronic states that are signatures of a quasi-trigonal planar carbamate species that is hydrogen bonded to an ammonium cation. This eliminates two of the three structures studied, and confirms the insertion mechanism. We note the particular sensitivity of X-ray absorption spectra to the insertion step of this mechanism, underpinning the strength of the technique for examining subtle chemical changes upon gas adsorption.

## 1 Introduction

Metal–organic frameworks (MOFs) have shown great potential for gas separation applications. In particular, MOFs featuring five-coordinate metal centers known as open metal sites are especially effective for separating $CO_2$ from dry gas mixtures.[1,2] The open metal sites act as Lewis acids and will preferentially adsorb $CO_2$ over $CH_4$ or $N_2$ with a moderate heat of adsorption that allows easy regeneration of the MOF *via* pressure or temperature swings. The MOF-74 series are among the most widely studied for this type of separation,[3–7] with Mg-MOF-74 being the highest-performing MOF of the experimentally studied series for $CO_2/N_2$ separations.[8–11]

Open metal site MOFs, however, operate *via* competitive adsorption and $CO_2$ preferentially binds over other guests like $N_2$. Unfortunately, this approach is not effective in the presence of water, since water binds more strongly than $CO_2$, limiting the effectiveness of such materials for capturing $CO_2$ from the flue gas streams of fossil-fuel-burning power plants.[12] Recently, it was demonstrated that mmen-$Mg_2$(dobpdc), an expanded variant of Mg-MOF-74 with diamines tethered to the open metal sites, addresses this limitation due to the ability of amines to adsorb $CO_2$ in the presence of $H_2O$ vapor.[13] Such supported amine adsorbents can mimic the well-known chemistry of a monoethanolamine (MEA) solution, while taking advantage of the low heat capacity of the solid material to reduce regeneration costs.[1,2] Furthermore, amines chemically bind only $CO_2$, not $H_2O$, eliminating adsorbent deactivation. The observed adsorption behavior for mmen-$Mg_2$(dobpdc) deviated drastically from the expected Langmuir-type behavior, however, displaying extremely high selectivity for $CO_2$ adsorption at low pressure *via* an unusual step-shaped adsorption isotherm.[13] The pressure at which this step occurs was found to change with temperature. This step-like adsorption behavior could be very useful for carbon

[a] *Materials Sciences Division, Lawrence Berkeley National Laboratory, Berkeley, CA 94720, USA. E-mail: jbkortright@lbl.gov*
[b] *Université Grenoble Alpes, Science et Ingénierie des Matériaux et Procédés (SIMAP), F-38000 Grenoble, France*
[c] *Department of Chemistry, University of California, Berkeley, California 94720, USA*
[d] *Molecular Foundry, Lawrence Berkeley National Laboratory, Berkeley, California 94720, USA*
[e] *Department of Chemical and Biological Engineering, University of California, Berkeley, California 94720, USA*
[f] *Department of Chemistry, Chemical Theory Center and Supercomputing Institute, University of Minnesota, Minneapolis, Minnesota 55455, USA*
† Electronic supplementary information (ESI) available. See DOI: 10.1039/c5cp02951a

 

capture applications: if a material can be designed such that it displays a step-shaped adsorption isotherm just below the relevant partial pressure of $CO_2$ in the gas mixture of interest, it could capture a larger amount of $CO_2$ per cycle with a significantly smaller temperature swing than traditional adsorbents, enabling a high efficiency separation with very low regeneration cost.

There was therefore great interest in understanding the molecular mechanism responsible for the unusual adsorption behavior in mmen-$Mg_2$(dobpdc),[14] which was elucidated using an assortment of complementary techniques, including *in situ* powder X-ray diffraction (XRD), *in situ* infrared (IR) spectroscopy, solid-state nuclear magnetic resonance (NMR) spectroscopy, *in situ* X-ray absorption spectroscopy (XAS), and density functional theory (DFT) computations. It was shown that $CO_2$ binds to the amines to form ammonium carbamate chains along the channels in the MOF, and displaces the amines at the open metal sites. In the absence of $CO_2$, one end of a given diamine is bound to an open metal site while the other end remains exposed. After $CO_2$ adsorption, the resulting carbamate is found to bind to the metal site through an oxygen atom, indicating that $CO_2$ inserts into the parent metal–nitrogen bond; to maintain charge pairing, ammonium carbamate pairs align in a highly ordered chain structure.[15] This structure is referred to here as the ''insertion structure''. The formation of the highly-ordered chains is responsible for the step-shaped isotherms, with long-range order only induced above a certain threshold pressure of $CO_2$ gas. This novel adsorption behavior, triggered by the insertion into the metal–nitrogen bond, shows great promise for a variety of high-capacity, low-cost $CO_2$ separations.

Herein, we present a more detailed XAS analysis of mmen-$Mg_2$(dobpdc) and mmen-$Mn_2$(dobpdc), exploring several potential binding configurations and explaining the observed spectra in terms of specific electronic excitations in the MOF that are only consistent with the aforementioned insertion structure. We employ *in situ* Near Edge X-ray Absorption Fine Structure (NEXAFS) spectroscopy at the N and O K-edges and the Mn L-edge to examine the electronic structure of the amines (and the Mn metal centers) as $CO_2$ adsorbs in these MOFs, as well as the electronic structure of the carbamate species formed upon adsorption. NEXAFS is an element-specific probe of the empty electronic states of a material, and is especially sensitive to structure and coordination near the excited atom. It is therefore highly sensitive to the chemistry and bonding configuration of the amines in the MOF as adsorption occurs, as well as to the binding configurations and structures of the adsorbed $CO_2$ molecules themselves. We have previously demonstrated the sensitivity of this technique to $CO_2$ adsorption at the open metal sites in Mg-MOF-74,[16] and here employ the same experimental procedure for mmen-$Mg_2$(dobpdc) and mmen-$Mn_2$(dobpdc). Our specially designed gas cell, detailed elsewhere,[16,17] allows cycling between vacuum and $CO_2$ gas environments for a MOF sample, revealing distinct and reproducible changes in the N and O K-edge spectra upon adsorption within each of the MOFs studied.

To understand the origin of these spectral signatures, we employ the eXcited electron and Core Hole (XCH) method to compute NEXAFS spectra of three DFT-optimized candidate geometries, identified as possible final configurations of the $CO_2$ uptake process.[15,16] These three configurations were chosen based upon previously computed structures that exhibit heats of adsorption comparable to experiment.[14,15,18] We then selected energetically favorable final geometries after DFT optimization to a local minimum in the potential energy landscape. In addition to the insertion structure mentioned above, we also examined the ''pairs structure'' and ''chain structure'', as depicted in Fig. 2 and discussed further below. The XCH method provides a detailed description of the individual electronic transitions underlying the NEXAFS spectra, including approximations of the final state wavefunctions that correspond to specific spectral features. As we will show, the NEXAFS spectra are sensitive to subtle differences in chemistry and bonding between these potential structures and provide compelling evidence for the insertion structure as the correct configuration.

# 2 Methods

## 2.1 Experimental

Measurements were performed at bending magnet beamline 6.3.2 ($10^{11}$ photons per s) at the Advanced Light Source, Lawrence Berkeley National Laboratory. We employed a custom gas cell that has been described in detail elsewhere,[16,17] and largely followed the same experimental procedure used to observe $CO_2$ adsorption in Mg-MOF-74,[16] except that the MOF samples were mounted on silicon carbide membranes rather than silicon nitride membranes to simplify spectral normalization for N K-edge spectra.

Transmission–absorption samples were prepared by suspending about 10 mg of mmen-$Mg_2$(dobpdc) or mmen-$Mn_2$(dobpdc) powder in $\sim$1 mL of dry hexanes and drop-casting the powder onto the surface of silicon carbide membranes (300 nm thickness). The membranes with deposited MOF powder were then loaded into a glass evacuation chamber and any guest species in the pores were purged by slowly evacuating the chamber, followed by heating to 100 °C for 4 h. These activated MOF samples were stored under dry nitrogen and loaded into the gas cell in a dry nitrogen glove box to ensure they were not exposed to air. The cell was then sealed and transported to the beamline for the NEXAFS measurements.[15]

NEXAFS spectra of mmen-$Mg_2$(dobpdc) at the N and O K-edges were collected in vacuum, representing the activated material. Spectra at the N K-edge were repeated under increasing pressures of $CO_2$ gas, to observe spectral changes as a function of adsorption. Oxygen K-edge spectra could not be collected with $CO_2$ gas in the cell as the resonant absorption from the free gas species obscured the spectrum of the MOF, but a final O K-edge spectrum was collected after evacuating the cell again. The $CO_2$ remained adsorbed in this material even after returning to vacuum at ambient temperature, so this final O K-edge spectrum includes contributions from the adsorbed $CO_2$ molecules. The same procedure was used for mmen-$Mn_2$(dobpdc), and Mn $L_{2,3}$-edge spectra were also collected in vacuum, at each pressure of $CO_2$, and in vacuum again after evacuating the gas.

Raw spectra were processed in the manner described previously,[16,17] using spectra of a blank silicon carbide membrane for background correction. After normalization and linear baseline subtraction, the intensities of the N K-edge spectra were scaled to 1 at 432.1 eV. Since the optical density at the O K-edge changed between initial and final spectra due to adsorbed $CO_2$, intensities of these spectra were not scaled, and therefore reflect the relative quantity of oxygen in each case. As before, care was taken to ensure that the X-ray beam spot did not move during measurement, such that the same portion of the powder sample was illuminated at each stage of the measurement and any spectral variance due to irregular sample morphology was minimized. Spectra were collected from 5 individual mmen-$Mg_2$(dobpdc) samples and 3 individual mmen-$Mn_2$(dobpdc) samples, with good reproducibility between samples.

### 2.2 DFT calculations

**(i) Structural optimization.** Atomic structures were relaxed based on evaluation of total energies and atomic forces from DFT calculations employing the generalized gradient approximation (GGA) of Perdew, Burke and Ernzerhof (PBE)[19] with the Grimme semi-empirical correction.[20] We use the localized atomic orbitals basis as implemented in the SIESTA package.[21] We employ a variationally optimized double-ζ polarized basis set for all atoms. Troullier–Martins pseudopotentials are used with 2s and 2p electrons for C, N and O explicitly included in the valence, while for Mg semicore electrons are considered. Real space integrals are performed using a mesh with 300 Ry cutoff. All geometries are fully optimized until Hellmann–Feynman forces are smaller than 0.03 eV $Å^{-1}$ and the stress tensor components are smaller than 0.2 kbar. The cell used for the activated structure contains 384 atoms, while the cells used for the pairs, chain and insertion structures include 420 atoms. These represent $1 \times 1 \times 2$ supercells of the hexagonal unit cells for each structure; cell dimensions are 21.7 Å × 21.5 Å × 14.2 Å for the activated and pairs structures, 21.7 Å × 21.7 Å × 13.7 Å for the chain structure, and 22.0 Å × 21.5 Å × 13.9 Å for the insertion structure.

**(ii) AIMD simulations.** The optimized structure of activated mmen-$Mg_2$(dobpdc) (384 atoms, $1 \times 1 \times 2$ supercell) obtained at 0 K was used as input to an AIMD simulation, performed using a modified version of the mixed Gaussian and plane wave code CP2K/Quickstep.[22,23] We employed a triple-ζ basis set with two additional sets of polarization functions (TZV2P)[24] and a 320 Ry plane-wave cutoff. The PBE functional is employed,[19] and the Brillouin zone is sampled at the $\Gamma$-point only. Interactions between the valence electrons and the ionic cores are described by norm-conserving pseudopotentials.[25,26] Solutions to the Poisson equation are provided by an efficient Wavelet-based solver.[27] We overcome the poor description of the long-range dispersive forces within the PBE-GGA exchange–correlation functional by employing the DFTD3 empirical corrections of Grimme *et al.*[28] We performed at least 50 ps of constant volume constant temperature (*NVT*) dynamics, saving a snapshot of the system (atomic coordinates and velocities) at every step. The temperature of the system was kept near 300 K using a Nose–Hoover thermostat (temperature damping constant of 100 fs). We used 8 uncorrelated snapshots as inputs when computing the NEXAFS spectra (see below).

The room temperature $CO_2$ insertion structures are obtained by performing constant-pressure (*NPT*) *ab initio* molecular dynamics simulations at 298 K. The Parrinello–Rahman barostat and Langevin thermostat[29,30] are used to control the pressure and temperature fluctuations, as implemented in the Vienna Ab Initio Simulation Package (VASP).[31,32] A timestep of 0.5 fs is used to update atomic positions and the corresponding electronic response. The projector-augmented wave (PAW) method[33,34] is used to describe the electron–ion interactions and the vdW-DF2 type non-local correlation functional[35] is used to treat the long-range dispersion relations in the system. The plane-wave basis set is truncated at 400 eV and the *k*-points are sampled on a $1 \times 1 \times 3$ uniform Monkhorst–Pack grid to ensure the electronic charge density is converged for a 210 atom simulation cell, representing the hexagonal unit cell for this structure. Again, we used 8 uncorrelated snapshots as inputs when computing the NEXAFS spectra (see below).

**(iii) Computed NEXAFS spectra.** The transition amplitudes are calculated according to the Fermi's golden rule expression for the X-ray absorption cross-section.[36] Within the electric-dipole approximation, we approximate the transition amplitudes as effective single-particle matrix elements, as detailed by Prendergast and Galli.[37] For the initial and final states we employ Kohn–Sham eigenstates of the ground and excited state self-consistent fields, respectively. The initial state is the 1s orbital of the O and N atoms and the final states are accessible (*i.e.*, unoccupied) Kohn–Sham eigenstates derived from a self-consistent field computed within the eXcited electron and Core-Hole (XCH) approximation for the electronic final state.[37]

The final state is computed self consistently using a core-excited pseudopotential for the excited atom and an additional extra electron to the total number of ground-state valence electrons. Starting from the transition amplitudes, the final spectra are computed using a Gaussian convolution of 0.3 eV for zero-Kelvin structures, and 0.2 eV for structures obtained from AIMD simulations. Additional details of the method have been described elsewhere.[16,38]

To interpret our spectra in terms of specific electronic states, we plot the core-excited electronic orbitals, resulting from inclusion of 1 core hole and an extra excited electron in the self-consistent field, as three-dimensional isosurfaces. This enables correlation of specific spectral features with the chemical bonding of the excited atom.

When computing N and O K-edge spectra for the AIMD calculations described above, eight representative AIMD snapshots were used in each case. For the insertion structure, each snapshot includes 6 diamines, for a total of 48 distinct samplings of the diamines and their coordination at 298 K; for the activated MOF the unit cell was doubled, providing 96 distinct samples of the diamines. For the insertion structure, this entails a total sampling of 96 nitrogen atoms (48 ammonium nitrogen atoms and 48 carbamate nitrogen atoms) and 240 oxygen atoms (48 metal-bound carbamate oxygen atoms, 48 hydrogen-bound carbamate

 

oxygen atoms, and 144 oxygen atoms in the organic linkers). For the activated structure, this entails a total sampling of 192 nitrogen atoms (96 metal-bound amines and 96 free amines) and 288 oxygen atoms in the organic linkers.

# 3 Results and discussion

## 3.1 NEXAFS measurements

Representative N K-edge spectra for mmen-$Mg_2$(dobpdc) are shown in Fig. 1a. Spectra were collected in vacuum and under increasing pressures of $CO_2$ gas, but only the initial vacuum spectrum and the spectrum at the highest pressure of $CO_2$ (36.1 Torr) are shown, so the spectral changes can be seen more clearly. The full pressure series of spectra are shown in Fig. S1 (ESI†). There are three major spectral changes, marked by red arrows: a new feature appears at 402.3 eV, the main edge peak at ~405.4 eV increases in intensity and blueshifts by ~1 eV, and a new, broad feature appears between 411 and 419 eV. Representative N K-edge spectra for mmen-$Mn_2$(dobpdc), shown in Fig. S2 (ESI†), reveal similar spectral changes, but they do not appear until higher gas pressures in accordance with the measured adsorption isotherm for this MOF.[13,15]

Representative O K-edge spectra for mmen-$Mg_2$(dobpdc) before and after $CO_2$ dosing are shown in Fig. 1b. The increased spectral intensity at high energy in the second spectrum reflects the increased oxygen density in the material after adsorption. The initial vacuum spectrum probes the organic dobpdc linkers in the MOF, with a prominent π* peak from the carboxylate groups at 532 eV. After dosing, a new π* feature appears at 532.9 eV. Nearly identical spectral signatures are observed for mmen-$Mn_2$(dobpdc), shown in Fig. S3 (ESI†).

Representative Mn L-edge spectra are shown in Fig. S4 (ESI†). No spectral changes are observed upon $CO_2$ adsorption. The Mn L-edge spectrum, however, only changes significantly at high crystal fields, when a transition from high to low spin occurs.[39] As long as the system remains in its high spin configuration, the Mn L-edge shows little sensitivity to the specific ligand geometry; even tetrahedral Mn complexes display nearly identical spectra to octahedral complexes.[40] Our measured spectra clearly show a high spin configuration throughout the $CO_2$ adsorption process, consistent with our previous report.[15] The spectra are therefore consistent with the adsorption process discussed further below.

## 3.2 Computed NEXAFS spectra

To explain and interpret our measured spectra, we computed NEXAFS spectra from three potential $CO_2$ adsorption configurations in mmen-$Mg_2$(dobpdc), shown in Fig. 2. The first configuration is called the "pairs structure", based on an earlier DFT study of this material.[14] In this structure, $CO_2$ binds to the free end of the amine to form a carbamic acid, which then forms hydrogen bonds with a neighboring carbamic acid, creating a carbamic acid pair. This pair can form across the MOF channel as previously reported,[14] or along the channel; in this study the pair that forms along the channel is used. The second

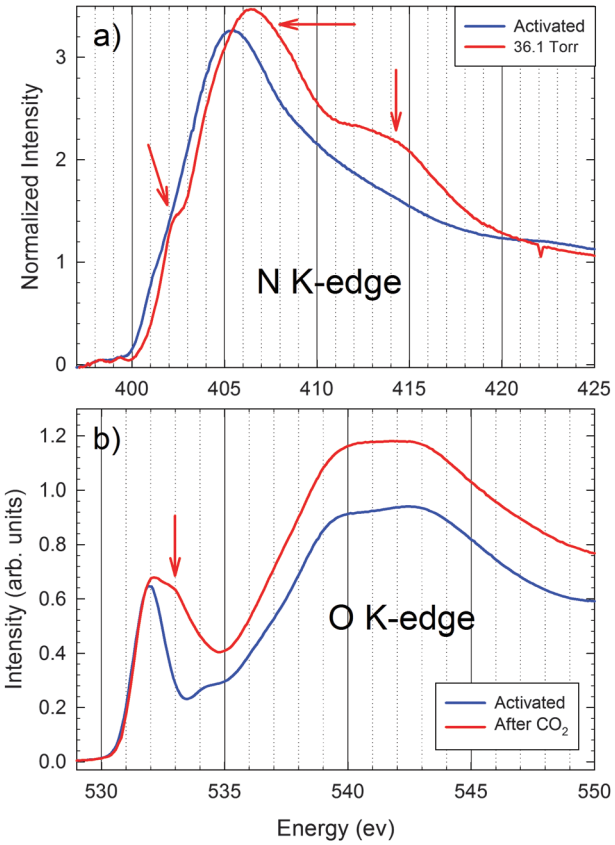


Fig. 1 (a) Representative N K-edge NEXAFS spectra of mmen-$Mg_2$(dobpdc) collected from a single sample in vacuum and at 36.1 Torr of $CO_2$ gas. The three major spectral changes are marked with red arrows: a new feature appears at 402.3 eV, the main edge at 405.4 eV increases in intensity and blueshifts by ~1 eV, and the new, broad feature appears between 411 and 419 eV. (b) Representative O K-edge NEXAFS spectra of the same sample of mmen-$Mg_2$(dobpdc) collected in vacuum before and after dosing with $CO_2$ gas. The generally increased intensity of the spectrum after dosing reflects the larger amount of oxygen present in the system after adsorption. A new π* peak appears at ~532.9 eV after adsorption, marked with a red arrow.

configuration is called the "chain structure" because the adsorbed $CO_2$ forms ammonium carbamate chains down the MOF channel. In this structure, $CO_2$ binds to the metal-bound end of the amine to form a carbamate, while a neighboring amine removes a proton to form an ammonium species. The carbamate and ammonium are stabilized by a combination of ionic and hydrogen bonding interactions. As each $CO_2$ molecule binds, ordered chains are formed, which may explain the step-like behavior of the adsorption isotherm. This binding mechanism may create either hydrogen-bound zwitterionic ammonium carbamate species as described above, or hydrogen-bound neutral carbamic acids and amines. Our DFT-optimized structure places the hydrogen involved in the hydrogen bond roughly equidistant from the ammonium (N···H = 1.23 Å) and carbamate species (O···H = 1.30 Å), creating a structure that is only slightly zwitterionic. The third configuration is the "insertion structure", which is formed in a similar manner as the chain structure but with a further step: as $CO_2$ adsorbs, it inserts into the metal–nitrogen bond, displacing the amine and forming a carbamate bound to

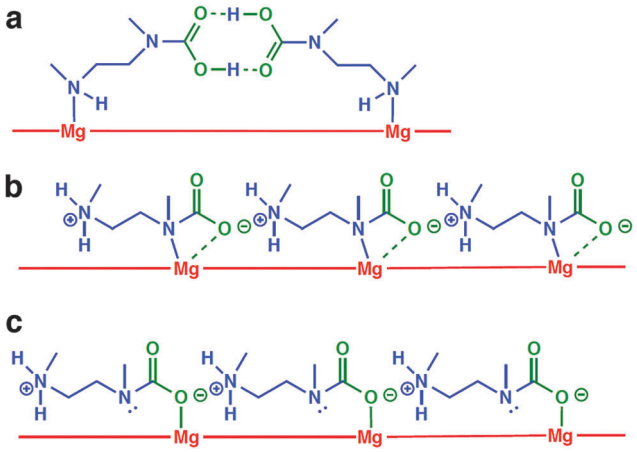


Fig. 2 (a) The "pairs structure". A $CO_2$ molecule binds to the free end of each amine, creating a carbamic acid which then forms a hydrogen bonded pair with its neighbor. (b) The "chain structure". $CO_2$ adsorbs to the metal-bound end of each amine, and the free end of each amine removes a hydrogen from its neighbor, creating ammonium carbamate (or neutral amine/carbamic acid) chains along the channels of the MOF. (c) The "insertion structure". Similar to the chain structure, except that the adsorbed $CO_2$ inserts into the metal–nitrogen bond, forming ammonium carbamate chains that are bound to the metals through the carbamate oxygen atoms.

the metal through the oxygen. Like the chain structure, the insertion structure can form either a zwitterionic or neutral configuration *via* a proton transfer, but structural relaxations of the saturated system indicate the zwitterionic form is the energetic minimum.[15] The insertion structure also creates ordered chains along the channels within the MOF and could therefore explain the step-like adsorption isotherm, as these chains do not form below a temperature-dependent threshold pressure.

We computed N and O K-edge spectra for activated mmen-$Mg_2$(dobpdc) and for the three structures illustrated in Fig. 2. A comparison of the computed N K-edge spectra for the activated MOF *versus* the three bound configurations is shown in Fig. 3. The pairs structure reproduces the new low-energy peak at ~402 eV, but does not reproduce the experimentally observed blueshift of the main edge peak at ~404 eV or the new, broad feature between 411 and 418 eV, while the chain structure has two weaker transitions near 402 eV and no blueshift of the main edge peak. The insertion structure, however, has a stronger peak near 402 eV, and the main edge at ~404 eV is blueshifted and increased in intensity, as observed in experiment. The insertion structure is also the only structure to reproduce the broad feature between 411 and 418 eV in the experimental spectrum.

Computed O K-edge spectra for all of the structures are also shown in Fig. 3. For the pairs structure, two new π* peaks appear at ~533 and ~534 eV upon $CO_2$ adsorption. These peaks correspond to the two O atoms of the carbamic acid moieties, one of which has a formal double bond and the other of which has a single bond and is protonated. While these would interconvert at ambient temperature, the fast timescale of the NEXAFS excitation (on the order of attoseconds, with a core-excited lifetime of femtoseconds) implies that the two distinct π* peaks would be distinguishable experimentally. In practice they would likely experience significant broadening, but even if merged into a single peak, the computed spectra suggest that this peak would appear at a higher energy than seen in experiment. The chain structure, on the other hand, shows a new π* transition overlapping that of the organic linkers, manifesting spectrally as a single peak that is broadened very slightly on the high energy side compared to the activated MOF. This contrasts with experiment. The insertion structure appears similar, but displays a larger blueshift in the π* peak. This is the closest to the experimental spectrum, but the blueshift is still smaller than that observed experimentally, possibly due to thermal effects (see below). The O K-edge spectra alone do not definitively rule out any of the structures, but when combined with the N K-edge spectra, they clearly show that the insertion structure is the best match to experiment. This is consistent with other experimental and theoretical characterization work reported previously, which eliminate the pairs structure and chain structure in favor of the insertion structure.[15]

There are still, however, significant qualitative differences between the experimental spectra and the computed spectra, likely due to thermal effects. In order to include thermal effects in our comparison, we approximated 298 K spectra for the activated MOF and the insertion structure using AIMD simulations as described in Section 2. The resulting spectra are shown in Fig. 4a and c. The separate spectral contributions from the carbamates and linkers are shown at the O K-edge in Fig. 4d, revealing that the blueshift of the π* peak arises entirely from the new carbamate moieties. These two moieties are more clearly resolved as two separate π* peaks in the experimental spectra than in the computed spectra; this may result from thermal effects that were not captured by our spectral calculations. The configurational sampling is necessarily limited by the significant computational cost of these calculations, so the full range of motion that exists in the real system may not be accurately represented in the computed spectra.

At the N K-edge, all three of the major spectral changes observed upon $CO_2$ adsorption remain in the 298 K computed spectra, but changes to intensities and spectral shapes provide a better qualitative match to experiment. The new feature at ~402 eV appears as a shoulder, as seen experimentally; the main edge at ~403.9 eV blueshifts by ~1 eV; and the new, broad feature appearing between 412 and 419 eV is retained at the higher temperature. These features, however, do not all appear at the experimentally observed energies. This is most noticeable for the main edge peak, which appears at ~403.9 eV in the computed spectrum for the activated MOF but at ~405.4 eV in the experimental spectrum for the activated MOF. The computed main edge peaks for both the activated MOF and the insertion structure are also narrower than in experiment. Typically, DFT-XCH estimates of K-edge spectra result in spectral features with an underestimated bandwidth with respect to experiment. This is often remedied using an empirical dilation of the simulated energy axis. However, in the present case, a dilation of 1.25 is already

 

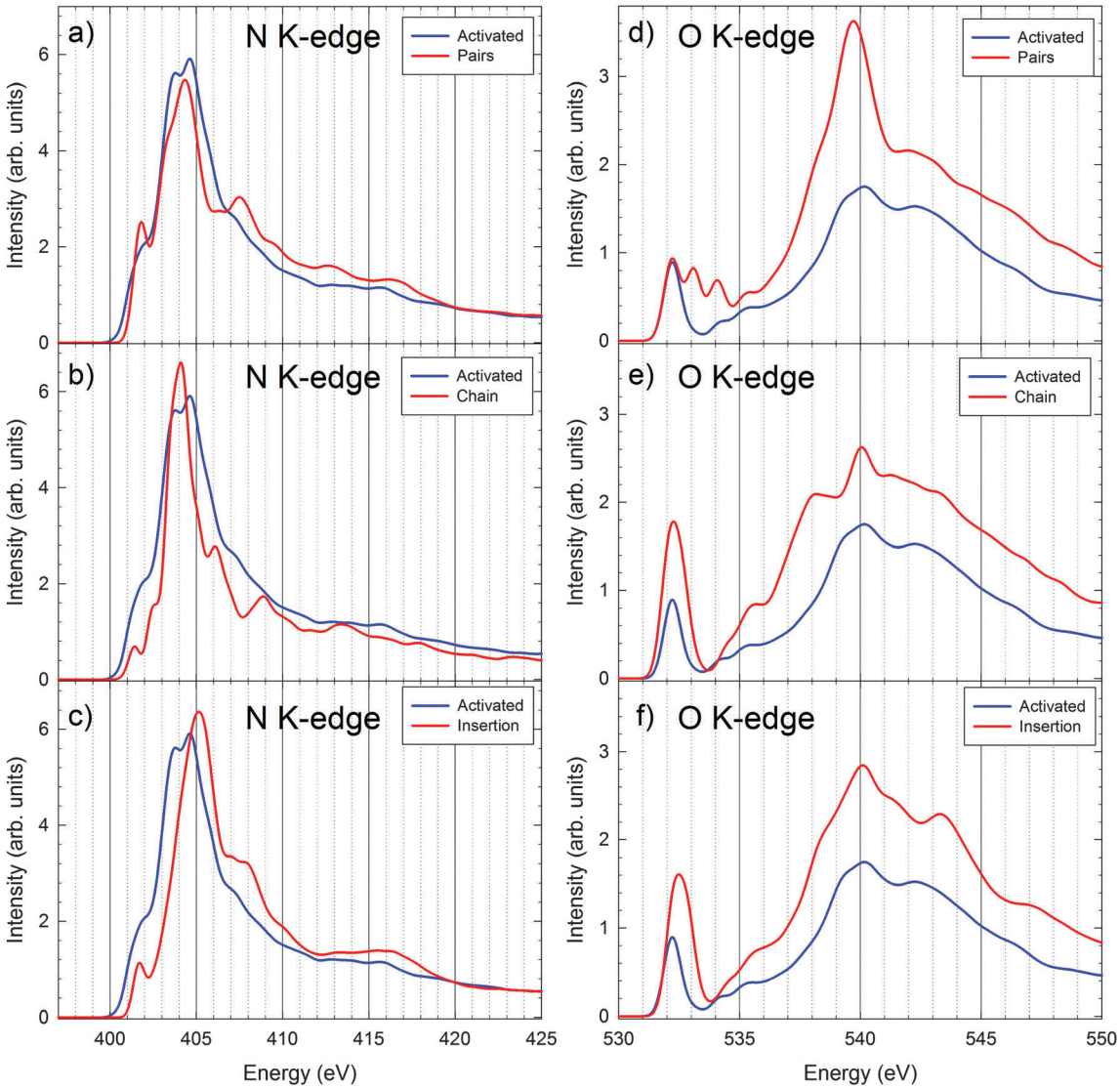


Fig. 3 Top row: Computed N K-edge (left) and O K-edge (right) spectra for the activated MOF and the pairs structure at zero K. The N K-edge spectra reproduce the new peak near 402 eV but not the blueshift or increase in intensity of the main edge at 404.5 eV. The O K-edge spectra show two new π* peaks at 533 and 534 eV. Middle row: Computed N K-edge (left) and O K-edge (right) spectra for the activated MOF and the chain structure at zero K. The N K-edge spectra do not show any of the experimentally observed changes. The O K-edge spectra show a slight broadening of the π* peak near 532 eV, in contrast to experiment. Bottom row: Computed N K-edge (left) and O K-edge (right) spectra for the activated MOF and the insertion structure at zero K. The N K-edge spectra for the insertion structure shows a new peak near 402 eV and an increase in intensity and blueshift of the main edge at 404.5 eV. The O K-edge spectra show a broadening and blueshift of the π* peak, implying a higher energy π* resonance from the adsorbed $CO_2$, but this cannot be resolved as a separate peak as it can in experiment.

included in our predicted spectra, so this cannot explain the observed spectral broadening. The differences between the experimental and computed spectra may be due in part to insufficient thermal sampling, as discussed above. Another possibility is that the electronic density of states generated from the DFT-XCH self-consistent field may not faithfully represent the relative alignment of all molecular orbital characters, and that the use of a different exchange–correlation functional (beyond semi-local PBE, using hybrid exact exchange) or corrections to the spectrum derived by many-body perturbation theory may correct this discrepancy, once they become computationally feasible.

To assist in explaining the origin of the spectral changes in the N K-edge spectra, we split the insertion structure spectrum into contributions from the carbamate N atoms and the ammonium N atoms, shown in Fig. 4b. This reveals that the new peak at ~402 eV arises entirely from the carbamate N atoms, as does the broad feature between 412 and 419 eV. The ammonium N atoms, however, are responsible for the blueshift of the main edge peak. This is consistent with a screening effect. The formal positive charges on the ammonium N atoms lead to deeper 1s core levels and larger NEXAFS transition energies, as seen in the spectrum. Therefore, the experimentally observed blueshift in the main edge peak implies an ammonium

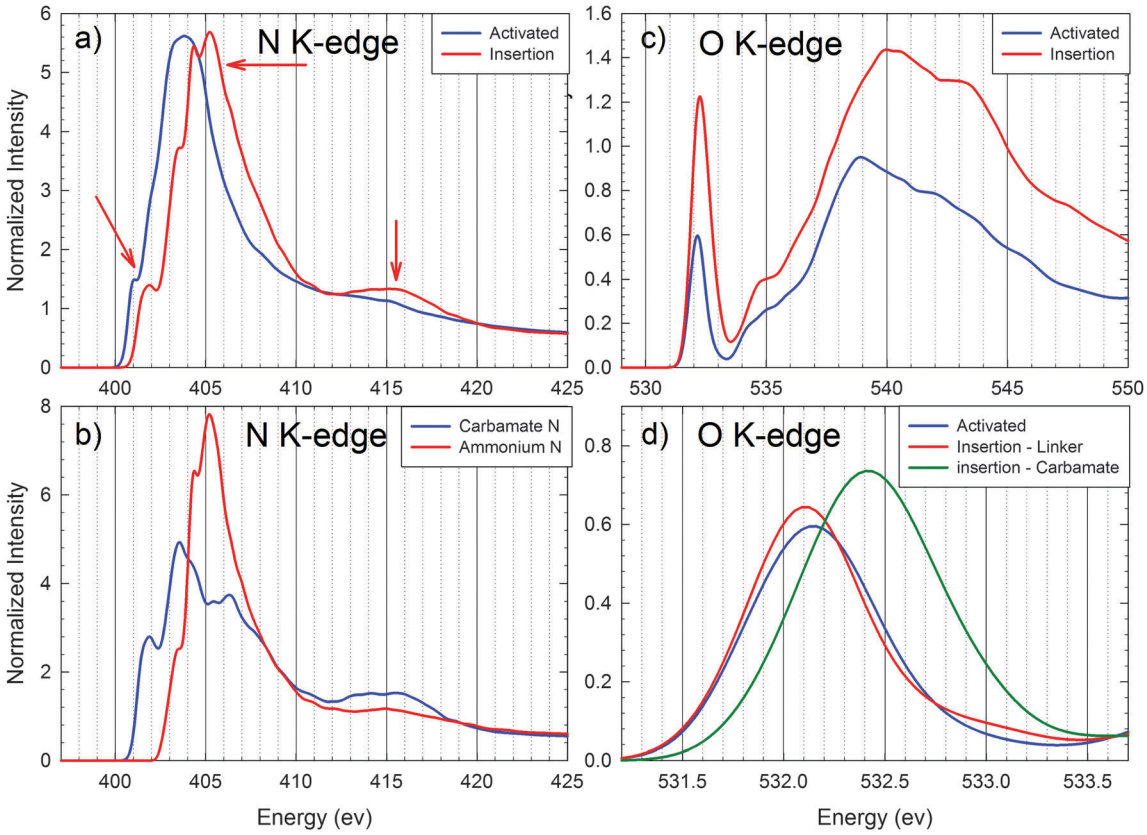


Fig. 4 (a) Computed N K-edge spectra for the activated MOF and insertion structure at 298 K. All three major spectral changes seen in experiment are reproduced, marked with red arrows: a new peak at 402 eV, a blueshift and increase in intensity of the main edge peak at 403.8 eV, and a new broad feature between 412 and 419 eV. (b) Computed N K-edge spectra for the insertion structure at 298 K, with contributions divided between carbamate N atoms and ammonium N atoms. The new peaks at 402 eV and 407.2 eV, as well as the broad feature between 412 and 419 eV, arise solely from the carbamate N atoms. The increase in intensity and blueshift of the main edge peak near 404 eV arises primarily from the ammonium N atoms. (c) Computed O K-edge spectra for the activated MOF and insertion structure at 298 K. New π* resonances from the adsorbed $CO_2$ appear at slightly higher energy, but not as high as in experiment. (d) A zoomed-in plot of the π* feature at the O K-edge, including contributions to the insertion structure spectrum from the linker O atoms and carbamate O atoms. The observed blueshift relative to the activated MOF arises entirely from the carbamates.

species; given the small zwitterionic character seen in the chain structure, ammonium only appears in significant quantity for the insertion structure.

Other spectral features can be analyzed by imaging the final state wavefunctions for the relevant transitions. The excited state electronic orbital densities corresponding to spectral features near 402 eV in the N K-edge spectra for each structure are shown in Fig. 5. In each case, these spectral features are associated with the carbamate N atoms. For the pairs structure, the wavefunction reveals a transition into the π* orbital of the carbamic acid. This is consistent with the quasi-trigonal planar configuration of the N, and the consequent presence of a π interaction with the carbamate. This transition is similar to that seen in N K-edge NEXAFS studies of amino acids upon formation of peptide bonds, in which a similar bonding configuration occurs with a trigonal planar nitrogen participating in the π system of a carbonyl group.[41,42] For the insertion structure, the peak at ~402 eV arises from a transition to a very similar final state, with a quasi-planar nitrogen coupled to the π* orbital of the carbamate. For the chain structure, however, the trigonal planar geometry of the carbamate N atom is broken, and its lone pair now forms a dative bond to the Mg center. This also manifests in a longer bond between the N and the carbamate (1.44 Å) compared to the shorter bonds in the pairs and insertion structures (1.37 and 1.41 Å, respectively). There is still some weak mixing with the π* of the carbamate group, but the transition intensity is very low due to the reduced hybridization.

The higher energy spectral features in the N K-edge spectrum of the insertion structure arise from transitions to σ* states associated with the new N–C bond in the carbamate. One such transition that contributes to the main edge peak at ~405 eV is shown in Fig. S5A (ESI†). Unlike the low-energy feature near 402 eV, the higher-energy spectral features consist of a large number of transitions. The broad feature between 412 and 419 eV arises from many transitions to σ* states which spans the entire unit cell of the MOF. These states show clear σ* character around the new N–C bond, so it appears that the increased spectral intensity in this region relative to the activated MOF is due to the formation of this bond. An example of one such state is shown in Fig. S5B (ESI†).

The final state wavefunctions corresponding to the π* transitions at the O K-edge for each structure are also shown in Fig. 5.

 

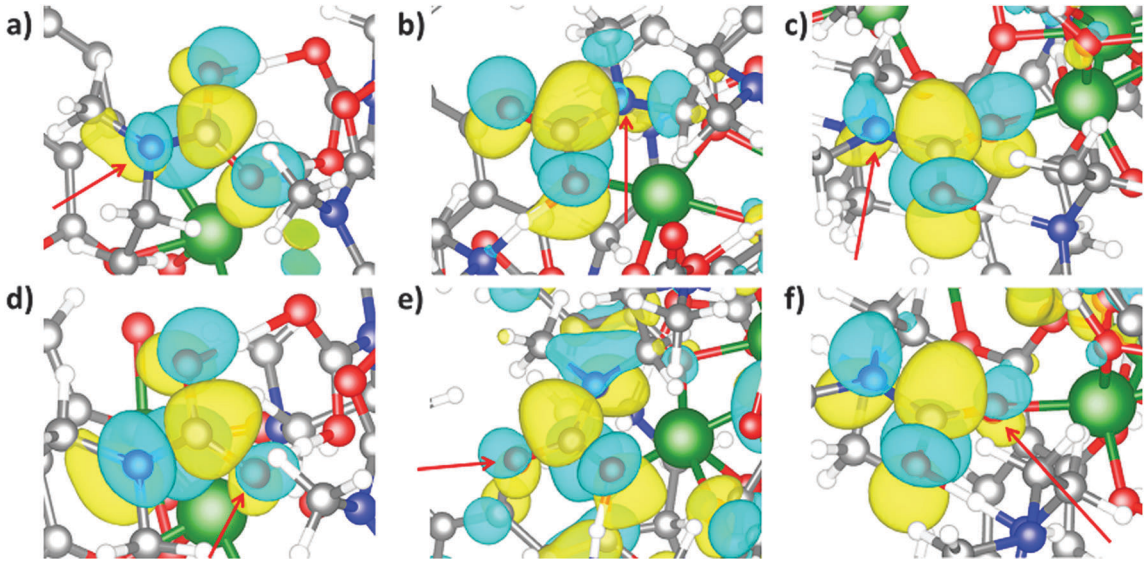


Fig. 5 Top row: Final state wavefunctions corresponding to the peak near 402 eV in the N K-edge spectra for the pairs structure (left), chain structure (center) and insertion structure (right). Red arrows indicate the excited atom in each case. Bottom row: Final state wavefunctions corresponding to the π* peak in the O K-edge spectra for the pairs structure (left), chain structure (center) and insertion structure (right). Red arrows indicate the excited atom in each case. These states closely resemble those in the top row, indicating a similar electronic structure accessed from both nitrogen and oxygen excitations.

Notably, these final states very closely resemble those seen near 402 eV in the N K-edge spectra. The final states primarily consist of the π* orbital of the carbamate or carbamic acid, with some contribution from the lone pair of the nitrogen. Unlike the N K-edge spectra, however, it is unclear if the coupling between the nitrogen and carbamate is responsible for the energy shift in the O π* transition. The pairs structure, for example, displays two new π* transitions rather than one, likely due to the hydrogen bonding configuration rather than the interaction with the N atom. The spectral differences between the chain and insertion structures, namely a blueshifted π* transition in the insertion structure as compared to the chain structure, are not as easily explained. This shift might arise from a screening effect, as seen for the peak near 405 eV in the N K-edge spectra, or it might reflect a changing final state energy, likely due to a different π–π* splitting energy for the insertion structure when compared to the chain structure. We applied full core hole (FCH) DFT calculations coupled with partial density of states (PDOS) calculations to quantify both the relative core level energies between the insertion and chain structures and the relative π–π* splittings for these structures (see ESI† for details). The PDOS calculations revealed that the π–π* splitting is nearly identical in each case, implying that the coupling of the nitrogen into the π* system in the insertion structure is not responsible for the shift in peak position relative to the chain structure. Rather, the FCH energies for the carbamate groups in the insertion structure show deeper core levels than those in the chain structure, likely due to an electron withdrawing effect from the direct Mg–O interaction in the insertion structure. Consequently the single, new blueshifted π* peak is a signature of insertion.

The primary spectral signatures of $CO_2$ adsorption in mmen-$Mg_2$(dobpdc) can therefore be explained in terms of the specific bonding occurring at the two nitrogen sites in each amine. The new N–C carbamate bond that forms between the initially metal-bound nitrogen and the adsorbed $CO_2$ molecule yields the broad, high-energy feature between 412 and 419 eV in the N K-edge spectrum, while the blueshift in the main edge peak at ~403.9 eV is due to the formation of ammonium groups on the free ends of the amines. The low-energy peak at ~402 eV is a signature of insertion, *i.e.* the displacement of the nitrogen at the metal site by the oxygen of the newly-formed carbamate. This frees the lone pair of the nitrogen to couple to the π system of the carbamate, creating this new transition at the N K-edge. While the pairs structure also shows this transition, it does not produce ammonium groups, and has been further discounted by *in situ* IR and solid-state NMR measurements.[15] Evidence for insertion is also seen in the O K-edge spectra, as new π* resonances appear at higher energy upon insertion due to the direct bond between the metal and the carbamate oxygen, as seen in experiment. McDonald *et al.* predicted that as $CO_2$ adsorbs in mmen-$Mg_2$(dobpdc), carbamates are formed first, followed by formation of the metal-bound carbamate (*i.e.*, insertion) product.[15] This is consistent with our experimental N K-edge spectra (Fig. S1, ESI†), which show the broad feature between 412 and 419 eV (a signature of the new carbamate bond) appearing first as gas is added to the cell, followed by the new peak at ~402.3 eV (a signature of insertion) at higher pressures.

## 4 Conclusion

Through *in situ* NEXAFS characterization of mmen-$Mg_2$(dobpdc) and mmen-$Mn_2$(dobpdc), we demonstrate strong spectral response to $CO_2$ adsorption in both materials at the N and O K-edges.

Careful computation of NEXAFS spectra of mmen-$Mg_2$(dobpdc) for three distinct binding configurations reveals the sensitivity of the spectra to the details of the bonding in the final structure. The experimental spectra clearly show the formation of an ammonium species as well as a carbamate. This carbamate must have a quasi-trigonal planar nitrogen, which creates a distinct pre-edge peak in the N K-edge spectrum through coupling of the free lone pair on the nitrogen with the $\pi^*$ orbital of the carbamate. This quasi-trigonal planar carbamate paired with an ammonium cation is achieved when the adsorbed $CO_2$ inserts into the metal–nitrogen bond, forming a carbamate bound to the metal directly through the oxygen and producing computed NEXAFS spectra in good qualitative agreement with experiment. This insertion also leads to the new, higher-energy $\pi^*$ resonance observed in the O K-edge spectra, by withdrawing electron density from the $\pi^*$ system. It is difficult to discern the insertion process with most characterization methods,[15] but it is very clear in the NEXAFS spectra, emphasizing the utility of the technique in determining subtle chemical differences and confirming proposed mechanisms.

Furthermore, the insertion mechanism explains the unusual step-shaped isotherm in these materials, and also provides insight into the design of adsorbents for specific applications.[15] Since insertion must occur and is dependent on the strength of the original metal–nitrogen and resulting metal–oxygen bonds, changing the identity of the metal centers and tuning the structure of the appended amines can shift the pressure at which the step occurs,[15] indicating a possible strategy for creating highly specialized adsorbents with very low regeneration costs for $CO_2$ separations.

## Acknowledgements

The work presented here was funded by the Center for Gas Separations Relevant to Clean Energy Technologies, an Energy Frontier Research Center funded by the United States Department of Energy (DOE), Office of Science, Office of Basic Energy Sciences under award DE-SC0001015. Work at SIMAP was performed using computer resources from the Grand Équipement National de Calcul Intensif (GENCI) under the Centre Informatique National de l'Enseignement Supérieur (CINES) grant 2014-c2015097211. The computational work performed by S.O.O. was supported through the Nanoporous Materials Genome Center of the DOE, Office of Basic Energy Sciences, Division of Chemical Sciences, Geosciences, and Biosciences, under award number DE-FG02-12ER16362. Experiments were performed at beamline 6.3.2 at the Advanced Light Source, and computations were performed as a user project at The Molecular Foundry, facilitated by T.P., L.F.W., C.D.P and D.P., including use of its computer cluster vulcan, managed by the High Performance Computing Services Group, and use of the National Energy Research Scientific Computing Center. These experiments and computations were performed at Lawrence Berkeley National Laboratory, which is supported by the Director, Office of Science, Office of Basic Energy Sciences, of the DOE under contract no. DE-AC02-05CH11231.

## References

1 D. M. D'Alessandro, B. Smit and J. R. Long, *Angew. Chem., Int. Ed.*, 2010, **49**, 6058–6082.
2 K. Sumida, D. L. Rogow, J. A. Mason, T. M. McDonald, E. D. Bloch, Z. R. Herm, T.-H. Bae and J. R. Long, *Chem. Rev.*, 2012, **112**, 724–781.
3 S. R. Caskey, A. G. Wong-Foy and A. J. Matzger, *J. Am. Chem. Soc.*, 2008, **130**, 10870.
4 P. D. C. Dietzel, V. Besikiotis and R. Blom, *J. Mater. Chem.*, 2009, **19**, 7362–7370.
5 Z. R. Herm, J. A. Swisher, B. Smit, R. Krishna and J. R. Long, *J. Am. Chem. Soc.*, 2011, **133**, 5664–5667.
6 Z. R. Herm, R. Krishna and J. R. Long, *Microporous Mesoporous Mater.*, 2012, **151**, 481–487.
7 D. Yu, A. O. Yazaydin, J. R. Lane, P. D. C. Dietzel and R. Q. Snurr, *Chem. Sci.*, 2013, **4**, 3544–3556.
8 D. Britt, H. Furukawa, B. Wang, T. G. Glover and O. M. Yaghi, *Proc. Natl. Acad. Sci. U. S. A.*, 2009, **106**, 20637–20640.
9 L. Valenzano, B. Civalleri, S. Chavan, G. T. Palomino, C. O. Arean and S. Bordiga, *J. Phys. Chem. C*, 2010, **114**, 11185–11191.
10 Z. Bao, L. Yu, Q. Ren, X. Lu and S. Deng, *J. Colloid Interface Sci.*, 2011, **353**, 549–556.
11 J. A. Mason, K. Sumida, Z. R. Herm, R. Krishna and J. R. Long, *Energy Environ. Sci.*, 2011, **4**, 3030–3040.
12 J. A. Mason, T. M. McDonald, T.-H. Bae, J. E. Bachman, K. Sumida, J. J. Dutton, S. S. Kaye and J. R. Long, *J. Am. Chem. Soc.*, 2015, **137**, 4787–4803.
13 T. M. McDonald, W. R. Lee, J. A. Mason, B. M. Wiers, C. S. Hong and J. R. Long, *J. Am. Chem. Soc.*, 2012, **134**, 7056–7065.
14 N. Planas, A. L. Dzubak, R. Poloni, L.-C. Lin, A. McManus, T. M. McDonald, J. B. Neaton, J. R. Long, B. Smit and L. Gagliardi, *J. Am. Chem. Soc.*, 2013, **135**, 7402–7405.
15 T. M. McDonald, J. A. Mason, X. Kong, E. D. Bloch, D. Gygi, A. Dani, V. Crocella, F. Giordanino, S. O. Odoh, W. S. Drisdell, B. Vlaisavljevich, A. L. Dzubak, R. Poloni, S. K. Schnell, N. Planas, K. Lee, T. Pascal, L. F. Wan, D. Prendergast, J. B. Neaton, B. Smit, J. B. Kortright, L. Gagliardi, S. Bordiga, J. A. Reimer and J. R. Long, *Nature*, 2015, **519**, 303–308.
16 W. S. Drisdell, R. Poloni, T. M. McDonald, J. R. Long, B. Smit, J. B. Neaton, D. Prendergast and J. B. Kortright, *J. Am. Chem. Soc.*, 2013, **135**, 18183–18190.
17 W. S. Drisdell and J. B. Kortright, *Rev. Sci. Instrum.*, 2014, **85**, 074103.
18 B. Vlaisavljevich, S. O. Odoh, S. K. Schnell, A. L. Dzubak, K. Lee, N. Planas, J. B. Neaton, L. Gagliardi and B. Smit, *Chem. Sci.*, 2015, DOI: 10.1039/C5SC01828E.
19 J. P. Perdew, K. Burke and M. Ernzerhof, *Phys. Rev. Lett.*, 1996, **77**, 3865–3868.
20 S. Grimme, *J. Comput. Chem.*, 2006, **27**, 1787–1799.
21 J. M. Soler, E. Artacho, J. D. Gale, A. Garcia, J. Junquera, P. Ordejon and D. Sanchez-Portal, *J. Phys.: Condens. Matter*, 2002, **14**, 2745–2779.
22 G. Lippert, J. Hutter and M. Parrinello, *Mol. Phys.*, 1997, **92**, 477–487.

23 J. VandeVondele, M. Krack, F. Mohamed, M. Parrinello, T. Chassaing and J. Hutter, *Comput. Phys. Commun.*, 2005, **167**, 103–128.
24 J. VandeVondele and J. Hutter, *J. Chem. Phys.*, 2007, **127**, 114105.
25 M. Krack, *Theor. Chem. Acc.*, 2005, **114**, 145–152.
26 S. Goedecker, M. Teter and J. Hutter, *Phys. Rev. B: Condens. Matter Mater. Phys.*, 1996, **54**, 1703–1710.
27 L. Genovese, T. Deutsch and S. Goedecker, *J. Chem. Phys.*, 2007, **127**, 054704.
28 S. Grimme, J. Antony, S. Ehrlich and H. Krieg, *J. Chem. Phys.*, 2010, **132**, 154104.
29 M. Parrinello and A. Rahman, *Phys. Rev. Lett.*, 1980, **45**, 1196–1199.
30 M. Parrinello and A. Rahman, *J. Appl. Phys.*, 1981, **52**, 7182–7190.
31 G. Kresse and J. Furthmuller, *Comput. Mater. Sci.*, 1996, **6**, 15–50.
32 G. Kresse and J. Hafner, *Phys. Rev. B: Condens. Matter Mater. Phys.*, 1993, **47**, 558–561.
33 P. E. Blochl, *Phys. Rev. B: Condens. Matter Mater. Phys.*, 1994, **50**, 17953–17979.
34 G. Kresse and D. Joubert, *Phys. Rev. B: Condens. Matter Mater. Phys.*, 1999, **59**, 1758–1775.
35 K. Lee, E. D. Murray, L. Kong, B. I. Lundqvist and D. C. Langreth, *Phys. Rev. B: Condens. Matter Mater. Phys.*, 2010, **82**, 081101.
36 J. Stöhr, *NEXAFS Spectroscopy*, Springer, New York, 1992.
37 D. Prendergast and G. Galli, *Phys. Rev. Lett.*, 2006, **96**, 215502.
38 A. H. England, A. M. Duffin, C. P. Schwartz, J. S. Uejio, D. Prendergast and R. J. Saykally, *Chem. Phys. Lett.*, 2011, **514**, 187–195.
39 F. M. F. de Groot, J. C. Fuggle, B. T. Thole and G. A. Sawatzky, *Phys. Rev. B: Condens. Matter Mater. Phys.*, 1990, **42**, 5459–5468.
40 G. van der Laan and I. W. Kirkman, *J. Phys.: Condens. Matter*, 1992, **4**, 4189–4204.
41 Y. Zubavichus, A. Shaporenko, M. Grunze and M. Zharnikov, *J. Phys. Chem. B*, 2007, **111**, 9803–9807.
42 Y. Zubavichus, A. Shaporenko, M. Grunze and M. Zharnikov, *Nucl. Instrum. Methods Phys. Res., Sect. A*, 2009, **603**, 111–114.